ROYAL SOCIETY
OF CHEMISTRY

PAPER

Check for updates

Continuous synthesis of 2,2,6,6-tetramethyl-4-piperidinol over CuCrSr/Al₂O₃: effect of Sr promoter†

Zijing Zhang‡,[abcd] Xi Chen‡,[e] Bowei Wang, [ID] *[abcd] Long Wang,[a] Yang Li, [ID] [acd] Xilong Yan [ID] [acd] and Ligong Chen [ID] *[abcd]

A continuous process was developed for catalytic hydrogenation of triacetoneamine (TAA) to 2,2,6,6-tetramethyl-4-piperidinol (TMP), both of which are indispensable raw materials of hindered amine light stabilizers. A series of promoter-modified CuCr/Al₂O₃ catalysts were prepared by co-precipitation method and evaluated by the above reaction. The effect of promoter on the catalytic performance was explored by characterization tools, in which, CuCrSr/Al₂O₃ exhibited excellent catalytic performance with nearly complete conversion of TAA and over 97% selectivity of TMP at 120 °C. The characterization results indicated that the doped Sr could decrease the size of Cu nanoparticles to provide more active sites, improve the ratio of Cu^+/Cu^0 to promote the adsorption of substrates, and reduce the surface acidity to depress side reactions, thus remarkably enhancing catalytic performance. This work provides a low-cost, reliable and efficient strategy for the continuous industrial production of TMP.

1. Introduction

Triacetoneamine (TAA, 2,2,6,6-tetramethyl-4-piperidone) and 2,2,6,6-tetramethyl-4-piperidinol (TMP) are the critical raw materials of hindered amine light stabilizers,[1,2] which have been used commonly in plastics, fibers, coatings, and rubbers.[3–6] However, TAA is easily oxidized at room temperature due to its thermo-sensitivity, and thus it is normally converted into the corresponding stable alcohol-TMP in industry.

As is well known, numerous methods have been reported for the production of TMP. Using sodium borohydride as a reducing agent, Wilson B. Lutz *et al.*[7] obtained TMP from TAA by chemical reduction. In addition, TAA could be reduced at the electrolyzer cathode, where E. Sh. Kagan *et al.*[8] synthesized TMP using the electrochemical method. However, these methods may cause pollution, and the small-scale production with high costs cannot meet the market demand. In order to overcome these deficiencies, the catalytic hydrogenation method was

developed for large-scale production.[9] Typically, Kintopf *et al.*[10] realized the synthesis of TMP in an autoclave over RANEY®-Ni, and further extended it to large-scale production. Notwithstanding, there were some drawbacks, including high energy consumption, the cumbersome separation and recycling of RANEY®-Ni, and flammable and explosive safety hazards.[9,11–15] Consequently, it is urgent to establish an economical, safety and convenient method to produce TMP. It will undoubtedly be of value to conduct research on continuous hydrogenation of TAA to TMP over cheap and efficient catalyst.

As reported and described in Scheme 1, the hydrogenation of TAA is quite complicated, consisting of a series of side reactions except for the target hydrogenation.[16–18] This is reasonably attributed to the unique chemical structure of TAA, and the blocked piperidine unit is prone to proceed catalytic hydrogenolysis.[19] Therefore, developing an efficient catalyst to realize the selective hydrogenation of TAA to TMP still remained a big challenge.

In our previous work, a continuous hydrogenation of TAA to TMP in a fixed bed reactor was reported, but the selectivity of TMP was not satisfied.[18] Moreover, with high metal content on basic alumina, the mechanical strength of shaped catalyst was poor. Thus, further work to improve the catalyst is required.

Based on the knowledge of complex hydrogenation reactions, not only the dispersion of metal nanoparticles, but some additional factors, such as the surface composition and acidity of catalysts, could also influence the catalytic activity and product selectivity.[20–23] Introducing appropriate promoters would boost the dispersion and modify the support thereby facilitating the progress of reactions.[20,24] However, there is little

[a] School of Chemical Engineering and Technology, Tianjin University, Tianjin 300350, P. R. China. E-mail: bwwang@tju.edu.cn; lgchen@tju.edu.cn

[b] Zhejiang Institute of Tianjin University, Shaoxing, Zhejiang 312300, P. R. China

*[c] Tianjin Engineering Research Center of Functional Fine Chemicals, Tianjin, P. R. China*

[d] Guangdong Laboratory of Chemistry and Fine Chemical Industry Jieyang Center, Guangdong Province 522000, P. R. China

[e] Institute of Pharmaceutical Sciences, China Pharmaceutical University, Nanjing 210009, P. R. China

† Electronic supplementary information (ESI) available. See DOI: https://doi.org/10.1039/d2ra08306j

‡ These authors contributed equally to this work.
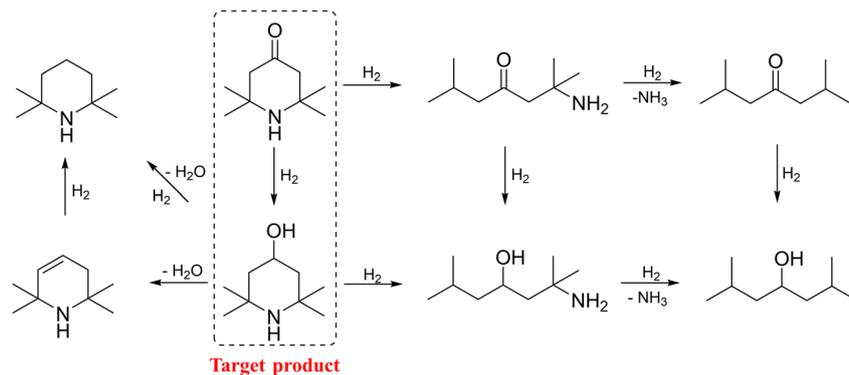
Scheme 1 A series of reactions for the hydrogenation of TAA.

research on the conversion from TAA to TMP and therefore not much information is available. According to our previous work and considering the service life of catalysts, we decided to use Al_2O_3 with desirable mechanical strength as carrier and introduce the third component to achieve this continuous hydrogenation process.

Herein, we developed a series of Cu-based catalysts by co-precipitation method with Al_2O_3 as support. The effect of promoter on its catalytic performance was explored, $CuCrSr/Al_2O_3$ was screened out and found to display the superior catalytic performance for the hydrogenation of TAA. Moreover, the prepared catalysts were characterized to explore the structure–activity relationship. The results revealed that the doped Sr markedly promoted the dispersion of Cu microcrystals, efficiently adjusted the surface composition of catalyst, and decreased the surface acidity, thus remarkably enhancing the catalytic performance and depressing side reactions. Furthermore, the reaction conditions were optimized, and under the optimized conditions, nearly quantitative conversion of TAA and over 97% selectivity of TMP were achieved.

2. Experimental section

2.1 Materials

2,2,6,6-Tetramethyl-4-piperidone (A.R.) was obtained by Adamas-Beta. $Cu(NO_3)_2 \cdot 3H_2O$ (A.R.), $Cr(NO_3)_3 \cdot 9H_2O$ (A.R.), $Sr(NO_3)_2$ (A.R.), $Zn(NO_3)_2 \cdot 6H_2O$ (A.R.), $Ce(NO_3)_3 \cdot 6H_2O$, $Mg(NO_3)_2 \cdot 6H_2O$ (A.R.), $Ca(NO_3)_2$ (A.R.), $Ba(NO_3)_2$ (A.R.) were purchased from Tianjin Guangfu Fine Chemical Research Institute, Tianjin, China. Na_2CO_3 (A.R.) was supplied by Tianjin Fengchuan Chemical Reagent Technology Co., Ltd., Tianjin, China. Pseudo-boehmite (99%, 300 mesh, $S_{BET} = 250$ m^2 g^{-1}, $V_{pore} = 0.40$ m^3 g^{-1}, A.R.) was obtained from Jiangsu Sanji Industrial Co., Ltd., Jiangyan, China. All commercially available reagents were used without further purification.

2.2 Catalyst preparation

The Cu-based catalysts were prepared using the co-precipitation method. The preparation of $CuCrSr/Al_2O_3$ (theoretical mass contents of the components: 20 wt% Cu, 5 wt% Cr, and 5 wt% Sr) was illustrated as following: 30.41 g $Cu(NO_3)_2 \cdot 3H_2O$, 15.39 g

$Cr(NO_3)_3 \cdot 9H_2O$ and 4.83 g $Sr(NO_3)_2$ were dissolved in 300 mL deionized water (solution A), and Na_2CO_3 solution was prepared as 1 mol L^{-1} (solution B). In a 2000 mL beaker, 300 mL of deionized water and 40.00 g pseudo-boehmite (equal to 28.00 g Al_2O_3) were introduced under mechanical stirring (>400 rpm). Then, solutions A and B were added dropwise simultaneously to the breaker. During the process, the pH of the mixture was kept around 8.0 using a pH meter. The resulting mixture was stirred for another 1 h and aged for further 12 h at room temperature. The precipitate was collected by filtration and washed with deionized water until the pH of the filtrate dropped to 7.0–7.5. The solid cake was dried at 110 °C for 6 h, crushed into 100 mesh powder, and then mixed with sesbania gum and deionized water to knead and extrude into bars with a diameter of 2 mm using an extruder. Eventually, the bars were dried at 110 °C for 6 h and calcined in a muffle furnace at 400 °C for 4 h. Before use, the catalysts were cut into small bars with a length of 3–5 mm and reduced in a stream of 1 MPa H_2 at 150 °C for 4 h.

Cu/Al_2O_3 and $CuCr/Al_2O_3$ were similarly prepared as above. In addition, $CuCrM/Al_2O_3$ catalysts were prepared by the same method with the same mass fraction (M: Zn, Ce, Ca, Mg or Ba; all were decomposed from their nitrates). Additionally, the catalysts with different Sr contents were expressed as $CuCrSr/Al_2O_3$-x (x represents the mass fraction of Sr, $x = 1, 3, 7$).

2.3 Characterization of catalysts

2.3.1 X-ray diffraction (XRD). This measurement was performed on an X'Pert Pro powder diffractometer (Panalytical, Netherlands) with a Cu Kα radiation source operating at 40 kV and a current of 40 mA in the range of 10°–100° (9° min^{-1}).

2.3.2 Transmission electron microscopy (TEM). It was performed using a JEOL JEM-F200 microscope operating at 200 kV. In addition, high-resolution transmission electron microscopy (HRTEM) observations and Energy Dispersive X-ray Spectroscopy (EDS) analyses were also carried out. Catalyst powder was dispersed in acetone and dripped on a microgrid supported by a molybdenum mesh.

2.3.3 Inductively coupled plasma optical emission spectrometer (ICP-OES). In order to analyze the element contents, an Agilent 730 ICP-OES spectrometer was used. The reduced catalyst sample was weighted and dissolved in a mixture of

HNO$_3$/HCl/HF (3 : 1 : 0.1, V/V). After the acid digestion at 300 °C for 2 h, the obtained solution was transferred into a 25 mL volumetric flask for the ICP-OES test.

2.3.4 Hydrogen temperature-programmed reduction (H$_2$-TPR). This analysis was carried out on a Micromeritics Autochem 2920 II instrument equipped with a thermal conductivity detector (TCD). To remove the adsorbed water and impurities, the catalyst powder (∼60 mg) was pretreated in an Ar gas stream (50 mL min^{-1}) at 300 °C for 2 h. After cooling to 30 °C, the sample was heated to 800 °C at a rate of 50 °C min^{-1} under the flow of H$_2$/Ar (1/9, v/v; 30 mL min^{-1}) gas mixture. The consumed amount of H$_2$ was monitored by a thermal conductivity detector (TCD). Calibration of TCD was performed by reduction of standard Ag$_2$O powder.

2.3.5 NH$_3$ temperature-programmed desorption (NH$_3$-TPD). NH$_3$-TPD was performed using a Micromeritics Autochem II 2920 instrument to investigate the acidity and acid amount of the catalyst. The unreduced catalyst sample (∼200 mg, ground into 40–60 mesh) was first pretreated in He gas stream (50 mL min^{-1}) at 300 °C for 2 h and H$_2$ (50 mL min^{-1}) at 150 °C for 4 h. After cooling to 50 °C, the NH$_3$ gas (50 mL min^{-1}) was introduced until saturation, followed by purging He (50 mL min^{-1}) for 1 h to remove physically absorbed NH$_3$. Finally, the sample was heated from 50 °C to 700 °C with a ramping rate of 10 °C min^{-1} under the flow of He (50 mL min^{-1}) gas.

2.3.6 X-ray photoelectron spectroscopy (XPS). XPS spectra were collected using an X-ray photoelectron spectrometer (K-Alpha+) with an Al Kα X-ray source for excitation. Before the measurement, the reduced catalysts were transferred to a vacuum vessel. The binding energy was calibrated using the C 1s peak (284.8 eV) as the reference.

2.3.7 N$_2$ adsorption–desorption measurements. The specific surface area was calculated according to the isotherms using the Brunauer–Emmett–Teller (BET) method. The pore volume and pore size were calculated using the BJH method according to the desorption branches of nitrogen isotherms.

2.4 Catalyst activity tests

The catalytic performance evaluation of Cu-based catalysts was carried out in a fixed-bed reactor with an inner diameter of 15 mm and a length of 650 mm, where 10 mL catalysts were charged. The schematic was shown in Fig. S1.† The reduced catalysts were obtained from calcined catalysts in a stream of 1 MPa H$_2$ at 150 °C for 4 h. 2,2,6,6-Tetramethyl-4-piperidone ethanol solution (20 wt%) was fed into the reactor by a syringe pump at a flow rate of 0.3 mL min^{-1}. The temperature of the reaction was monitored by a thermocouple placed in the middle of the reactor. The reaction mixture was cooled by condenser and collected, which was then analyzed once an hour by a gas chromatograph equipped with PEG-20M (30 m × 0.5 mm) capillary column and FID detector. The components of sample were quantified by area normalization method. The program was carried out from 80 to 240 °C at a rate of 15 °C min^{-1} with a constant N$_2$ flow at 50 mL min^{-1}. The measured results were averaged for data credibility, and the mass difference between reaction product and feed was lower than 3% for six hours. The reaction sample was qualitatively analyzed by Agilent 6890/5975 gas chromatography-mass spectrometry (GC-MS) equipped with an HP-5 capillary column (30 m × 0.5 mm) and an FID detector with a relative standard deviation of less than 2%. The conversion of raw materials and selectivity of products were calculated according to the following equations:

$$\text{Conversion (\%)} = \left(1 - \frac{\text{Molar amount of raw after reaction}}{\text{Molar amount of raw before reaction}}\right) \times 100$$

$$\text{Selectivity (\%)} = \left(\frac{\text{Molar amount of one product after reaction}}{\text{Molar amount of raw converted}}\right) \times 100$$

3. Results and discussion

3.1 Catalytic performance

As illustrated above, several Cu-based catalysts were successfully prepared, and then employed in the continuous hydrogenation of TAA to TMP in a fixed-bed reactor. The obtained results are summarized in Table 1. Under 100 °C, only TMP product was detected in the reaction mixture, and the conversion of TAA was enhanced by the introduction of chromium and different third metal elements, such as 45.19%, 53.55% and the best 75.21% TAA conversions achieved over Cu/Al$_2$O$_3$, CuCr/Al$_2$O$_3$ and CuCrSr/Al$_2$O$_3$ respectively. Compared with Cu/Al$_2$O$_3$ and CuCr/Al$_2$O$_3$, the third component (such as Zn, Ce, and alkaline-earth metals) in the catalysts exhibited different

Table 1 Hydrogenation reaction of TAA over Cu-based catalysts

Entry	Catalyst	Conversion/%	Selectivity/%		
			TMP	DIBK	Others
1[a]	Cu/Al$_2$O$_3$	45.19	100	—	—
2[a]	CuCr/Al$_2$O$_3$	53.55	100	—	—
3[a]	CuCrZn/Al$_2$O$_3$	48.08	100	—	—
4[a]	CuCrCe/Al$_2$O$_3$	50.75	100	—	—
5[a]	CuCrMg/Al$_2$O$_3$	67.62	100	—	—
6[a]	CuCrCa/Al$_2$O$_3$	57.92	100	—	—
7[a]	CuCrSr/Al$_2$O$_3$	75.21	100	—	—
8[a]	CuCrBa/Al$_2$O$_3$	68.61	100	—	—
9[b]	Cu/Al$_2$O$_3$	60.26	90.56	8.34	1.10
10[b]	CuCr/Al$_2$O$_3$	61.60	92.77	6.45	0.78
11[b]	CuCrZn/Al$_2$O$_3$	57.55	93.12	6.14	0.74
12[b]	CuCrCe/Al$_2$O$_3$	58.96	91.65	7.63	0.72
13[b]	CuCrMg/Al$_2$O$_3$	80.43	94.10	5.11	0.79
14[b]	CuCrCa/Al$_2$O$_3$	81.79	93.55	4.97	1.48
15[b]	CuCrSr/Al$_2$O$_3$	86.70	95.86	3.21	0.93
16[b]	CuCrBa/Al$_2$O$_3$	83.53	93.41	5.64	0.95

[a] Reaction conditions: 10 mL catalysts, 100 °C. [b] Reaction conditions: 10 mL catalysts, 120 °C, 2 MPa hydrogen, feed rate of TAA ethanol solution = 0.3 mL min^{-1} (20%).

catalytic performances. Although Zn and Ce were reported to be efficient cocatalysts of Cu-based catalysts in hydrogenation reactions,[24,25] none of them achieved better results in the above reaction. Encouragingly, it was found the doped alkaline-earth metals can effectively promoted TAA conversion. Except for a slight increase in the conversion of TAA over CuCrCa/Al$_2$O$_3$, other catalysts all acquired significant improvements, among which CuCrSr/Al$_2$O$_3$ showed the best.

Considering the insufficient reaction at 100 °C, further exploration was performed at 120 °C. When the hydrogenation temperature was elevated to 120 °C, TAA conversion increased. However, in addition to TMP, 2,6-dimethyl-4-heptanone (DIBK), 2-amino-2,6-dimethyl-4-heptanone, 2,6-dimethyl-4-heptanol and other byproducts were detected. CuCrSr/Al$_2$O$_3$ catalyst still presented the best TAA conversion of 86.70% and TMP selectivity of 95.86%, exhibiting outstanding catalytic performance.

As discussed above, the doped element can importantly influence the catalytic activity of Cu based catalysts, and doping with alkaline earth metals was an effective way to improve CuCr/Al$_2$O$_3$. To gain further insights into the structure–catalytic performance relationship of the obtained catalysts, they were fully characterized as following.

3.2 Characterization of catalysts

The X-ray diffraction patterns for calcined and reduced Cu/Al$_2$O$_3$, CuCr/Al$_2$O$_3$, and CuCrSr/Al$_2$O$_3$ were shown in Fig. 1A and B, respectively. The characteristic peaks of CuO (located at $2\theta = 35.5°, 38.7°, 38.9°, 48.7°, 61.5°$) and γ-Al$_2O_3$ (located at $2\theta = 39.5°, 45.9°, 66.9°, 80.6°, 85.0°$) were obviously observed in Fig. 1A, and the diffraction peaks located at 25.2°, 25.9°, 36.3°, 36.7°, 44.2°, and 47.9° were assigned to SrCO$_3$ phase of CuCrSr/Al$_2$O$_3$. Besides, no diffraction peaks were attributed to Cr or Cu–Cr oxides in calcined CuCr/Al$_2$O$_3$ and CuCrSr/Al$_2$O$_3$ catalysts, indicating that Cr particles were small or amorphous. It is noteworthy that the characteristic peaks of CuO became broader and weaker with the doping of Cr and Sr, indicating the better dispersion of CuO particles. In addition, the characteristic peaks of Al$_2$O$_3$ also became broader in CuCrSr/Al$_2$O$_3$, implying that the doped Sr regulated the property of Al$_2$O$_3$ carrier. After reduction, the diffraction peaks of CuO

disappeared and the characteristic peaks of metallic Cu (located at $2\theta = 43.3°, 50.4°, 74.1°, 89.9°, 95.1°$) appeared in Fig. 1B. In addition, the rest diffraction peaks in Fig. 1B were basically similar as those peaks in Fig. 1A. With the doping of Cr and Sr, the similar behavior of peaks of Cu in reduced catalysts was observed as that of CuO, suggesting a smaller particle size of Cu in CuCrSr/Al$_2$O$_3$. The particle sizes of Cu calculated by Debye–Scherrer equation were 19.5, 17.1, and 9.5 nm for Cu/Al$_2$O$_3$, CuCr/Al$_2$O$_3$, and CuCrSr/Al$_2$O$_3$, respectively. This result indicated that Sr promoted the dispersion and reduced the size of Cu nanoparticles.

The distributions of Cu nanoparticles in Cu/Al$_2$O$_3$, CuCr/Al$_2$O$_3$, and CuCrSr/Al$_2$O$_3$ were also investigated using TEM, as shown in Fig. 2. Black particles were irregularly distributed on bulk Al$_2$O$_3$ support of Cu/Al$_2$O$_3$ and CuCr/Al$_2$O$_3$, suggesting the poor dispersion of Cu species. With the doping of Sr, the aggregation of metal particles was suppressed. Besides, the further statistical analysis showed that the size of Cu particles decreased from 25.8 nm over Cu/Al$_2$O$_3$ to 23.7 nm over CuCr/Al$_2$O$_3$, and even to 9.4 nm over CuCrSr/Al$_2$O$_3$, implying that doped Sr can markedly improve the dispersion of Cu particles, which squared well with the result of XRD. Thus, more active sites in CuCrSr/Al$_2$O$_3$ were provided for the hydrogenation of TAA to TMP.

To further reveal the structure and elemental distribution of CuCrSr/Al$_2$O$_3$, HRTEM and EDS elemental mapping (Fig. 3) were employed. As shown in HRTEM image of Fig. 3, well-resolved crystalline lattice spacings of about 0.213 nm were associated with the (1 1 1) planes of metallic Cu. The EDS elemental mapping results of CuCrSr/Al$_2$O$_3$ displayed homogeneous distributions of Cu, Cr, Sr, Al, and O. It should be noted that the distribution of Cr was consistent with that of Cu while Sr was uniformly distributed on the catalyst, which indicated that Cr and Sr might play different roles. It seemed that there was an interaction between Cu and Cr species[26] while Sr species were more likely to interact with the carrier of catalysts to enhance the Cu species dispersion, and both of them could promote the catalytic activity. In addition, the interaction between Sr and carrier also reasonably demonstrated the change of Al$_2$O$_3$ peaks in Fig. 1A.

The unreduced catalysts were characterized by H$_2$-TPR to investigate the reduction behavior, as shown in Fig. 4. It mainly
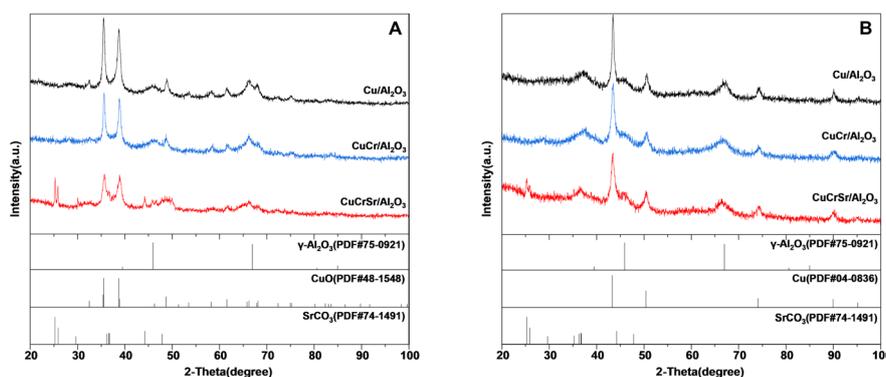

Fig. 1 XRD patterns of Cu/Al$_2$O$_3$, CuCr/Al$_2$O$_3$ and CuCrSr/Al$_2$O$_3$ after (A) calcination and (B) reduction.
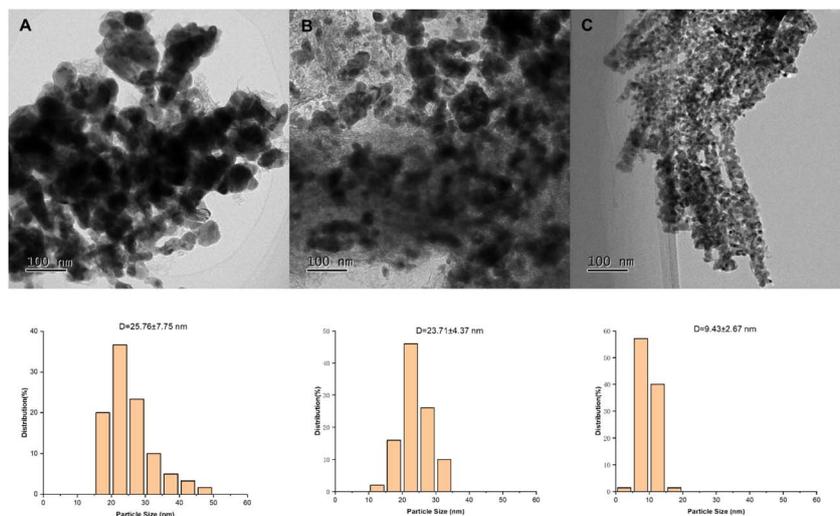
Fig. 2   TEM images of catalysts after reduction. ((A) Cu/Al$_2$O$_3$; (B) CuCr/Al$_2$O$_3$; (C) CuCrSr/Al$_2$O$_3$)

revealed the reduction characteristics of CuO because Cr and Sr species could not be reduced under this condition. In each case, a strong hydrogen reduction peak was found, which is the typical profile for Cu^{2+} to Cu^0.[27] For Cu/Al$_2$O$_3$ catalyst, the reduction peak occurred at 249 °C. And as for unreduced CuCr/Al$_2$O$_3$, the reduction peak shifted to 220 °C. This result indicated that the introduction of Cr improved the reducibility of CuO. CuCrSr/Al$_2$O$_3$ sample exhibited similar reduction behavior as CuCr/Al$_2$O$_3$ but at a lower temperature of 218 °C, suggesting that the doped Sr could further improve the reducibility of CuO. Not only did the reduction temperature drop, but the area of the reduction peak also decreased gradually with the addition of Cr and Sr, which could imply some kind of change in the surface compositions.[28]

To reveal the surface compositions and chemical states of Cu/Al$_2$O$_3$, CuCr/Al$_2$O$_3$, and CuCrSr/Al$_2$O$_3$, XPS spectra were collected and shown in Fig. 5. For all reduced catalysts, Cu 2p$_{3/2}$ peak at 932.0 eV and Cu 2p$_{1/2}$ peak at 952.0 eV were observed, and attributed to Cu^0 and/or Cu$^+$ species.[29,30] With the addition of Cr, Cu 2p peaks moved to lower binding energy ($\sim$931.8 eV),

indicating the obvious interaction between Cu and Cr,[20,31] which was consistent with EDS mapping analysis results. The binding energy of Cu 2p peak after further adding Sr was comparable to that of CuCr/Al$_2$O$_3$, slightly less than that of Cu/Al$_2$O$_3$. In addition, the fine spectra of Cu/Al$_2$O$_3$ and CuCr/Al$_2$O$_3$ by Gaussian
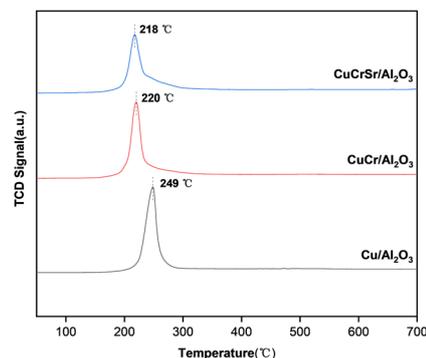
Fig. 4   H$_2$-TPR profiles of Cu/Al$_2$O$_3$, CuCr/Al$_2$O$_3$, CuCrSr/Al$_2$O$_3$ after calcination.
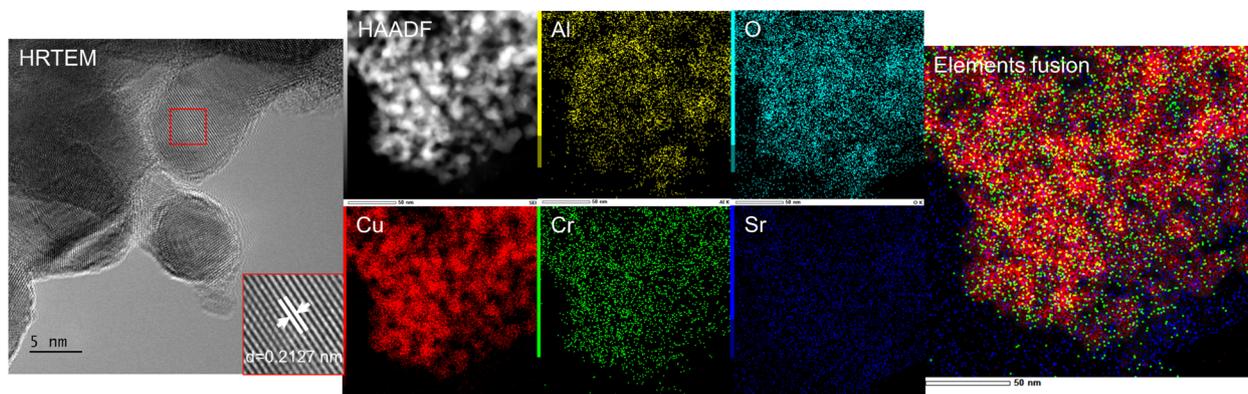

Fig. 3   HRTEM, HAADF, and EDS mapping images of CuCrSr/γ-Al$_2$O$_3$ (elements fusion diagram was composed by Cu, Cr, and Sr).
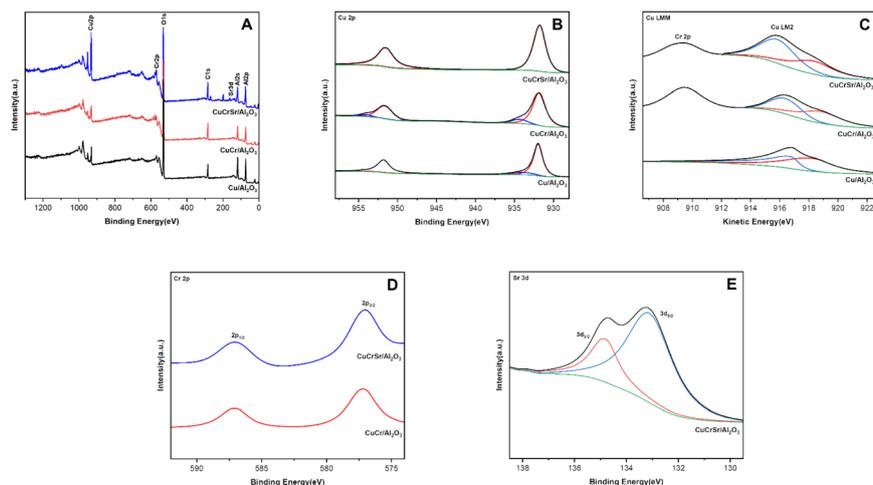
Fig. 5 (A) XPS survey, (B) Cu 2p, (C) Cu LMM Auger, (D) Cr 2p, and (E) Sr 3d spectra of Cu-based catalysts after reduction.

peak fitting exhibited shoulder peaks accompanying Cu $2p_{3/2}$ and Cu $2p_{1/2}$ at higher binding energy, suggesting the existence of Cu^{2+}, which was probably due to the oxidation of metallic Cu during the testing process. Besides, no Cu^{2+} was detected in $CuCrSr/Al_2O_3$. Because of the similar binding energy of Cu^0 and Cu^+ species, it was difficult to distinguish them only by XPS analysis of Cu 2p peaks. In order to confirm the exact chemical state of Cu species on catalysts, we adopted Cu LMM XAES to clarify this (Fig. 5b). In the Cu LMM spectra, based on deconvolution and Gauss fitting, the Auger peaks could be fitted into two peaks, the lower kinetic energy corresponding to Cu^+ species and the higher corresponding to Cu^0 species.[20,31] Numerical proportion results were listed in Table S1.† It was found that the proportion of Cu^+ gradually increased with the introduction of Cr and Sr, which could reasonably explain why the areas of reduction peaks decreased gradually in Fig. 4. As reported, the existence of Cu^+ could favor the adsorption of substrates.[32]

Fig. 5d showed the Cr 2p spectrum in $CuCr/Al_2O_3$ and $CuCrSr/Al_2O_3$. The binding energies of 577.1 eV and 587.0 eV were matched with Cr $2p_{2/3}$ and Cr $2p_{1/2}$, respectively, implying that Cr species existed in +3 valence state.[33] As for the Sr 3d spectrum of $CuCrSr/Al_2O_3$ in Fig. 5e, the peaks could be deconvoluted into two peaks located at 134.1 eV and 135.9 eV,

corresponding to Sr $3d_{5/2}$ and Sr $3d_{3/2}$, indicating the successful Sr-doping in $CuCr/Al_2O_3$.[34]

NH_3-TPD was carried out to characterize the surface acidity of reduced Cu-based catalysts. As shown in Fig. 6, all the catalysts presented three NH_3 desorption peaks, suggesting there were three kinds of acid sites on the surface of catalysts. The first peak located at 0–200 °C was assigned to weak acid sites, and the second peak at 200–350 °C was associate with medium-strong acid sites, while the third peak located at 350–500 °C was attributed to strong acid sites.[35,36] As for weak acid sites, all of the catalysts displayed comparable strength of peak around 110 °C. For the medium-strong acid peaks, compared with Cu/Al_2O_3, the peak of $CuCr/Al_2O_3$ shifted to a lower temperature, but it became broader and larger. Furthermore, $CuCrSr/Al_2O_3$ presented the lowest quantity of medium-strong acidic sites. In the case of strong acid sites, the strength and amount gradually decreased with the doping of Cr and Sr. Obviously, all types of acid sites decreased significantly with the addition of Sr, which might alter its adsorption capacity for TAA and TMP.

Moreover, the physicochemical properties of Cu-based catalysts were investigated and summarized in Table S2.† ICP-OES results indicated that the actual compositions of all catalysts were close to the predetermined values. N_2 adsorption–desorption isotherms and pore size distribution of all samples (Fig. S2†) confirmed the presence of mesoporous structures, which showed characteristic IV isotherms with H_3-type hysteresis loops. As the addition of Cr and Sr, BET surface area, pore volume, and pore size of the catalyst presented a decreasing trend, which indicated that the additives were deposited in the pores probably.
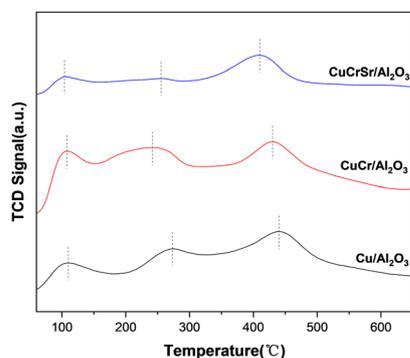
3.3 Condition optimization

Reaction conditions would impose great influences on the reaction. Therefore, the catalytic performance of $CuCrSr/Al_2O_3$ catalyst for the hydrogenation of TAA was further investigated. Catalysts containing different Sr amounts were designed to explore the effect of doped Sr, and the results were shown in Fig. 7A. When the amount was 1%, the catalytic activity was just
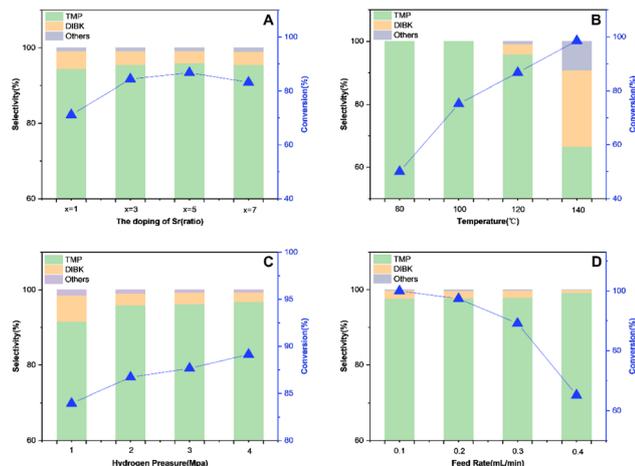

Fig. 6 NH_3-TPD profiles of Cu-based catalysts after reduction.

Fig. 7 (A) Catalytic results over CuCrSr/Al$_2$O$_3$-x. Reaction conditions: 10 mL catalyst, 120 °C, 2 MPa hydrogen, feed rate of TAA ethanol solution = 0.3 mL min^{-1} (20%). (B) Catalytic results over CuCrSr/Al$_2$O$_3$ at different temperature. Reaction conditions: 10 mL catalyst, 2 MPa hydrogen, feed rate of TAA ethanol solution = 0.3 mL min^{-1} (20%). (C) Catalytic results over CuCrSr/Al$_2$O$_3$ at different hydrogen pressure. Reaction conditions: 10 mL catalyst, 120 °C, feed rate of TAA ethanol solution = 0.3 mL min^{-1} (20%). (D) Catalytic results over CuCrSr/Al$_2$O$_3$ at different feed rate. Reaction conditions: 10 mL catalyst, 120 °C, 4 MPa hydrogen.

a little improvement. As the amount gradually increased, 5 wt% Sr content catalyst exhibited the best conversion of TAA and selectivity of TMP. However, further increase in Sr content led to a decreased TAA conversion compared with CuCrSr/Al$_2$O$_3$-5, which implied excessive Sr caused a negative impact. This might be due to the blocking of pore structure by Sr species. Thus, 5 wt% was selected as the optimum Sr content.

Additional tests were carried out to evaluate the effect of reaction conditions. The catalytic performance of CuCrSr/Al$_2$O$_3$ catalyst was further investigated concerning reaction temperature (Fig. 7B), H$_2$ pressure (Fig. 7C) and feed rate (Fig. 7D).

As shown in Fig. 7B, the conversion of TAA exhibited a gradual increase from 80 (58%) to 140 °C (99%). However, higher reaction temperature would also cause more by-products like DIBK. When the temperature was raised to 140 °C, TMP

selectivity dropped to 67%. Thus, 120 °C was determined as the optimal hydrogenation temperature.

Fig. 7C showed the effect of hydrogen pressure. TAA conversion increased from 83.95% at 1 MPa hydrogen pressure to 89.13% at 4 MPa, suggesting the positive effect of increasing hydrogen pressure. TMP selectivity was poor at 1 MPa H$_2$, and it raised with increasing hydrogen pressure. Here the optimal hydrogen pressure was set as 4 MPa.

As illustrated in Fig. 7D, different feed rates were adopted. The highest conversion was obtained when the feed rate was 0.1 mL min^{-1}. And with further increase of the feed rate, the conversion decreased gradually. On the contrary, TMP selectivity increased slightly with the change of feed rate.

Overall, the final optimum conditions were 120 °C, 4 MPa hydrogen pressure, and 0.1 mL min^{-1} feed rate. At this point TAA conversion and TMP selectivity were 99.99% and 97.67%, respectively.
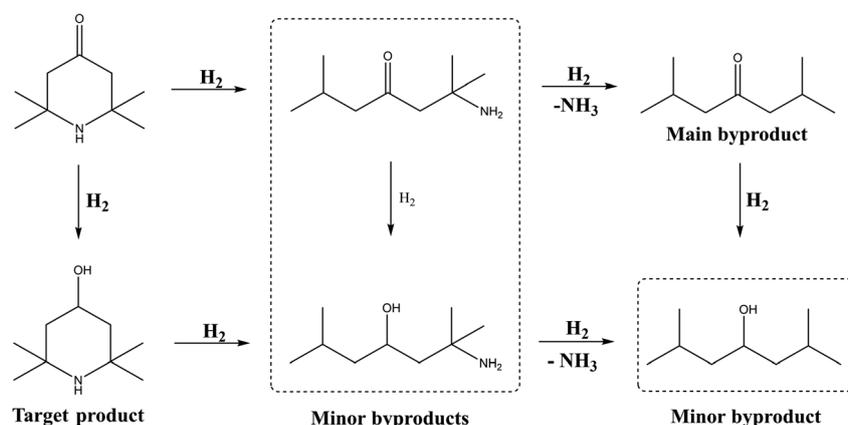
3.4 Reaction pathway

As reported and explored above, a plausible reaction pathway of TAA hydrogenation to TMP was described in Scheme 2. The hydrogenation to C=O was the major reaction under the optimized conditions, but several byproducts were detected in the reaction mixture, among which 2,6-dimethyl-4-heptanone was the major one. Considering the amino group is bonded to two tertiary carbon atoms and the uneven electron cloud distribution would weaken the C–N bonds, thus it is easy to undergo catalytic hydrogenolysis reaction.[37] Moreover, the acidic sites of Al$_2$O$_3$ could adsorb TAA and TMP molecules and further enhanced the catalytic cracking of the C–N bond.[19] These factors indicated that it was quite difficult to achieve full selectivity towards target TMP.

According to NH$_3$-TPD results, the doped Sr could effectively decrease the acid strength and amount of Al$_2$O$_3$, so efficiently inhibit the adsorption of TAA and TMP molecules, and suppress the catalytic hydrogenolysis of C–N bond.

3.5 Catalyst stability

Service life is one of the important indexes to evaluate the performance of a catalyst. The long-term stability result over

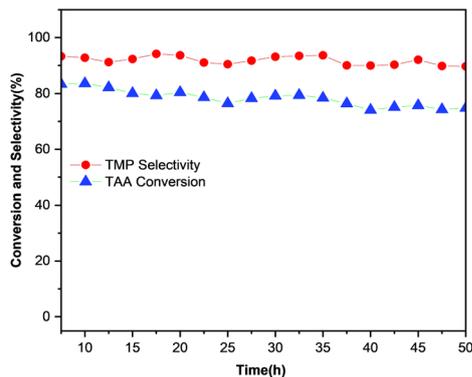Scheme 2 Plausible reaction pathway of TAA hydrogenation.

Fig. 8 Time on stream performance of CuCrSr/Al$_2$O$_3$. Reaction conditions: 6 mL catalysts, 120 °C, 4 MPa H$_2$, flow rate of TAA ethanol solution = 0.2 mL min^{-1} (20%).

CuCrSr/Al$_2$O$_3$ catalyst under the moderate reaction conversions was described in Fig. 8. It was apparent that TAA conversion stayed at around 80% while TMP selectivity remained over 90% at 120 °C for 50 h, demonstrating the good stability of this catalyst. What's more, no fragmentation or loss of catalysts was observed during the reaction process. Compared with Cu$_{30}$Cr$_5$/Basic Alumina in our previous work, CuCrSr/Al$_2$O$_3$ exhibited better mechanical strength during the hydrogenation. To further study the stability of CuCrSr/Al$_2$O$_3$, XRD patterns and TEM images of the used catalyst were collected. The consistent patterns of fresh and used catalysts in Fig. S3† demonstrated its crystal structure remained unchanged after the reaction. Moreover, no significant aggregation of nanoparticles was discovered in TEM image of the used catalyst, although the average nanoparticle size in the used catalyst increased slightly from 9.5 to 11.0 nm. These results all confirmed the excellent stability of CuCrSr/Al$_2$O$_3$ catalyst.

3.6 Structure–activity correlation

Analysis of catalyst structure–activity relationship is essential for the understanding of catalysis and catalyst design. Generally, high dispersion of the active metal species was crucial for improving catalytic activity.[38] The well-dispersed Cu nanoparticles on the catalyst could provide more active sites and improve the contact efficiency of hydrogenation to yield target TMP. According to the characterization results, the decreased size of CuCrSr/Al$_2$O$_3$ nanoparticles was evident compared with Cu/Al$_2$O$_3$ and CuCr/Al$_2$O$_3$. This would be the main reason for the excellent catalytic performance of TAA hydrogenation.

Moreover, the surface compositions and chemical states of Cu-based catalysts would also influence the catalytic performance.[32] According to XPS results, the amount of Cu$^+$ proportion increased with the introduction of Sr. Typically, Cu$^+$ species could act as sites for adsorption and activation of C=O bond.[32,39] Thus, the increased amount of Cu$^+$ proportion could facilitate the reaction process. Besides, Cu^0 species are generally regarded as the sites for activating and dissociating hydrogen for hydrogenation reactions.[40] Therefore, we can infer that the

rational proportion of Cu^0 and Cu$^+$ was one of the reasons for enhancing catalytic effectiveness.

Furthermore, the doped Sr not only promoted the dispersion of Cu and affected the electronic state of surface Cu species, but also regulated the surface acidic sites on the catalyst. As previously analyzed, the surface acidity might cause the adsorption of TAA and TMP molecules and break the C–N bond, leading to the generation of byproducts. Based on NH$_3$-TPD characterization, the surface acidity environment of CuCrSr/Al$_2$O$_3$ catalyst was significantly diminished by doped Sr, which would reduce the occurrence of side reactions to a certain extent and boost the hydrogenation reaction. This might be one of the reasons why CuCrSr/Al$_2$O$_3$ catalyst showed excellent selectivity.

To sum up, these discussions demonstrated that the catalytic activity towards TMP was not only related to highly dispersed Cu, but also associated with the surface compositions and suitable acidity of catalysts.

4. Conclusions

In this work, we have developed a continuous process of TAA to TMP over CuCrSr/Al$_2$O$_3$. Complete TAA conversion and 97.67% TMP selectivity were obtained. The characterization results revealed that the doped Sr promoted the dispersion of Cu, adjusted the surface compositions, and diminished the surface acidity of the catalyst. The nanoparticle size of CuCrSr/Al$_2$O$_3$ decreased from 25.8 to 9.5 nm, which provided more active sites and improved the contact efficiency of hydrogenation. Introducing Sr could adjust the proportion of Cu$^+$/Cu^0, and the rational proportion would promote the adsorption of substrates and catalytic performance. Besides, the doped Sr decreased the acid strength and amount of Al$_2$O$_3$, which inhibited the adsorption and catalytic cracking of the C–N bond in TAA and TMP molecules, thus reducing the occurrence of side reactions. The catalyst showed excellent stability in long-term test. These results were beneficial to the development of efficient and stable Cu based catalysts for production of TMP.

Conflicts of interest

There are no conflicts to declare.

Acknowledgements

Notes and references

1 F. A. Wang, J. Zhu, J. Song, S. Zhai and L. Wang, *Molecules*, 2001, **6**, 528–532.
2 M. A. Chinelatto, J. A. M. Agnelli and S. V. Canevarolo, *Polímeros*, 2015, **25**, 575–580.
3 R. V. Todesco and N. Ergenc, *Chimia*, 2002, **56**, 225.
4 F. Gugumus, *Polym. Degrad. Stab.*, 1994, **44**, 273–297.

5   C. Schaller, D. Rogez and A. Braig, *J. Coat. Technol. Res.*, 2009, **6**, 81–88.

6   R. d. Chai and J. Zhang, *Polym. Eng. Sci.*, 2013, **53**, 1760–1769.

7   W. B. Lutz, S. Lazarus and R. I. Meltzer, *J. Org. Chem.*, 1962, **27**, 1695–1703.

8   E. Sh. Kagan, I. A. Avrutskaya, S. V. Kondrashov, V. T. Novikov, M. Ya. Fioshin and V. A. Smirnov, *Chem. Heterocycl. Compd.*, 1984, **20**, 288–289.

9   M. Irfan, T. N. Glasnov and C. O. Kappe, *ChemSusChem*, 2011, **4**, 300–316.

10 K. Siegfried, *DE pat.*, 2656764A1, 1997.

11 K. D. Mukherjee, I. Kiewitt and M. Kiewitt, *J. Am. Oil Chem. Soc.*, 1975, **52**, 282–288.

12 D. Liu, D. Zemlyanov, T. Wu, R. J. Lobo-Lapidus, J. A. Dumesic, J. T. Miller and C. L. Marshall, *J. Catal.*, 2013, **299**, 336–345.

13 K. Wilson, *Appl. Organomet. Chem.*, 2007, **21**, 1002.

14 G. Ertl, H. Knözinger, F. Schüth and J. Weitkamp, *Handbook of Heterogeneous Catalysis*, Wiley-VCH, 2008.

15 G. V. Smith and F. Notheisz, *Heterogeneous catalysis in organic chemistry*, Academic, 1999.

16 S. Kuniko, *JP pat.*, 2002001118A, 2002.

17 R. Membrat, A. Vasseur, D. Moraleda, S. Michaud-Chevallier, A. Martinez, L. Giordano and D. Nuel, *RSC Adv.*, 2019, **9**, 37825–37829.

18 J. Ma, S. Liu, X. Fan, X. Du, X. Yan and L. Chen, *Chin. J. Catal.*, 2012, **33**, 605–609.

19 R. Prins, Y. Zhao, N. Sivasankar and P. Kukula, *J. Catal.*, 2005, **234**, 509–512.

20 Y. Zeng, B. Wang, W. Xu, X. Yan, Y. Li, G. Bai and L. Chen, *Catal. Sci. Technol.*, 2022, **12**, 2084–2096.

21 A. Saadi, Z. Rassoul and M. M. Bettahar, *J. Mol. Catal. A: Chem.*, 2000, **164**, 205–216.

22 F. Dong, Y. Zhu, H. Zheng, Y. Zhu, X. Li and Y. Li, *J. Mol. Catal. A: Chem.*, 2015, **398**, 140–148.

23 F. Dong, G. Ding, H. Zheng, X. Xiang, L. Chen, Y. Zhu and Y. Li, *Catal. Sci. Technol.*, 2016, **6**, 767–779.

24 X. Cai, Y. Ke, B. Wang, Y. Zeng, L. Chen, Y. Li, G. Bai and X. Yan, *Mol. Catal.*, 2021, **508**, 111608.

25 C. P. Jiménez-Gómez, J. A. Cecilia, F. I. Franco-Duro, M. Pozo, R. Moreno-Tost and P. Maireles-Torres, *Mol. Catal.*, 2018, **455**, 121–131.

26 K. Yan and A. Chen, *Energy*, 2013, **58**, 357–363.

27 J. J. Bravo-Suárez, B. Subramaniam and R. V. Chaudhari, *Appl. Catal., A*, 2013, **455**, 234–246.

28 M. Konsolakis and Z. Ioakeimidis, *Appl. Surf. Sci.*, 2014, **320**, 244–255.

29 M. C. Biesinger, *Surf. Interface Anal.*, 2017, **49**, 1325–1334.

30 M. C. Biesinger, L. W. M. Lau, A. R. Gerson, R. St and C. Smart, *Appl. Surf. Sci.*, 2010, **257**, 887–898.

31 C. Lin, J. Li, H. Guo, X. Wu, B. Wang and X. Yan, *Catal. Commun.*, 2018, **111**, 64–69.

32 A. Li, D. Yao, Y. Yang, W. Yang, Z. Li, J. Lv, S. Huang, Y. Wang and X. Ma, *ACS Catal.*, 2022, **12**, 1315–1325.

33 B. P. Payne, M. C. Biesinger and N. S. McIntyre, *J. Electron Spectrosc. Relat. Phenom.*, 2011, **184**, 29–37.

34 R. P. Vasquez, *J. Electron Spectrosc. Relat. Phenom.*, 1991, **56**, 217–240.

35 Z. Yu, F. Meng, Y. Wang, Z. Sun, Y. Liu, C. Shi, W. Wang and A. Wang, *Ind. Eng. Chem. Res.*, 2020, **59**, 7416–7425.

36 L. Chen, T. V. W. Janssens, M. Skoglundh and H. Grönbeck, *Top. Catal.*, 2019, **62**, 93–99.

37 K. Ouyang, W. Hao, W.-X. Zhang and Z. Xi, *Chem. Rev.*, 2015, **115**, 12045–12090.

38 K. Zhou, X. Sun, Y. Muhammad, P. Hu, Y. Li, Z. Tong and Z. Zhao, *Appl. Catal., A*, 2018, **555**, 138–147.

39 X. Yuan, S. Chen, D. Cheng, L. Li, W. Zhu, D. Zhong, Z.-J. Zhao, J. Li, T. Wang and J. Gong, *Angew. Chem.*, 2021, **133**, 15472–15475.

40 Y. Zeng, B. Wang, F. Yan, W. Xu, G. Bai, Y. Li, X. Yan and L. Chen, *ChemCatChem*, 2022, **14**, e202200311.